The Schrödinger-Poisson Selfconsistency in Layered Quantum Semiconductor Structures

by

Jonathan Edward Moussa

A Thesis

Submitted to the Faculty

of the

WORCESTER POLYTECHNIC INSTITUTE

in partial fulfillment of the requirements

for the Degree

of Master of Science

in

Physics

October 24, 2003

APPROVED:

Dr. L. Ramdas Ram-Mohan, Major Advisor

Dr. T. H. Keil, Head, Physics Department

Abstract

We develop a selfconsistent solution of the Schrödinger and Poisson equations in semiconductor heterostructures with arbitrary doping profiles and layer geometries. An algorithm for this nonlinear problem is presented in a multiband $\mathbf{k} \cdot \mathbf{P}$ framework for the electronic band structure using the finite element method. The discretized functional integrals associated with the Schrödinger and Poisson equations are used in a variational approach. The finite element formulation allows us to evaluate functional derivatives needed to linearize Poisson's equation in a natural manner. Illustrative examples are presented using a number of heterostructures including single quantum wells, an asymmetric double quantum well, *p*-*i*-*n*-*i* superlattices and trilayer superlattices.

Acknowledgements

I would mainly like to thank Professor Ram-Mohan for guiding and mentoring me for the past five years. Because of his dedication to my learning what it means to do research, I am now a more thoughtful planner of long term projects, and a very competent independent-minded researcher.

I wish to thank Professor Keon-Ho Yoo for his help with setting up the examples calculated in this thesis and for many discussions.

I would also like to thank the Air Force Research Laboratory at the Wright Patterson Air Force Base for their hospitality over two summers.

I wish to thank Quantum Semiconductor Algorithms, Inc., for the use of their finite element and sparse matrix analysis software.

This work was supported by Professor Ram-Mohan's grant from the National Science Foundation (Grant ECS-0084512) and the grant under the DARPA SpinS program (ONR Grant N00014-00-1-0951).

A manuscript based on this work has been submitted for publication in a journal.

Contents

Abstract i

Acknowledgements ii

1. Introduction 1

2. Schrödinger's equation 4

2.1. A finite element formulation 4

2.2. Boundary and interface conditions in the FEM 7

3. Poisson's equation 9

3.1. The source terms 10

3.2. Selfconsistency iterations 13

3.3. Finite element implementation 15

4. Applications 21

4.1. multi-band $\mathbf{k} \cdot \mathbf{P}$ model and selfconsistency 21

4.2. Further considerations 22

4.3. Results 23

4.3.1. A single quantum well with p-type modulation doping 24

4.3.2. A p-type modulation-doped asymmetric double quantum well 25

4.3.3. p-i-n-i superlattices 25

4.3.4. n-type modulation-doped trilayer superlattices 26

4.3.5. Effect of finite temperature 27

5. Concluding Remarks 28

Bibliography 30

1. INTRODUCTION

In modulation doped semiconductor heterostructures, the presence of discontinuities in the band edges leads to the possibility of the separation of the carriers from their parent donors or acceptors. This redistribution of the free carriers, together with the presence of ionized impurities in so-called depletion regions, gives rise to a selfconsistent reconfiguration of the band edges. As is well known, this problem is numerically unstable because small changes in the potential profile lead to substantial rearrangements of free carriers. The carriers are free in the sense that they are ionized away from the impurity atoms, though they could be bound within quantum wells, for example.

Here we present a selfconsistent solution of the spatial behavior of the energy band edge in arbitrary layered semiconductor nanostructures. For illustrative purposes and to describe the algorithm, we first consider the case of donor impurities and conduction band carriers in a single energy band model, and later treat the multiband case. The carrier charge density is determined by the solution of Schrödinger's equation for the wavefunctions of the carriers in the layered quantum system. This is introduced into Poisson's equation as a source term together with the positive charge distribution of ionized donors. The resulting potential arising from the redistributed charges is obtained by solving Poisson's equation. This potential alters the initial band edge potential with flat bands, and Schrödinger's equation is solved once again for the new total potential energy. This cycle of solving the two differential equations is iterated to convergence. We do not include any polarization charges due to stress-induced piezoelectric or spontaneous polarization in the layers. Also, we do not consider structures with Type-II energy band gap alignments that have semimetallic (zero band gap) properties, though Type-II structures with open band gaps are amenable to this analysis.

We have utilized the finite element method (FEM) for the solution of both Schrödinger's and Poisson's equations. Both of these equations are solved by employing the principle of least action.[1–3] Being a time-independent problem, this reduces to making the Lagrangian stationary to variations. In our modeling of structures with high doping, we find that the convergence is substantially faster in FEM in terms of the number of iterations and stability, even for doping concentrations as high as $10^{21}\,\mathrm{cm}^{-3}$, than conventional finite difference methods based on the shooting approach.[4]

Almost all earlier work has focused on specific structures, such as single interfaces between semiconductor materials,[5, 6] single quantum wells, bilayer superlattices,[7] or double barrier resonant tunneling structures.[8] The single symmetric quantum well with modulation doping in the barriers was treated by us earlier in a finite element framework,[1, 9] but the algorithm was specialized to that particular case.

The present method borrows from the recent work by Trellakis, *et al.*,[10] who solve the selfconsistency problem for a two-dimensional distribution of carriers with finite difference methods. We specifically consider layered III-V semiconductor structures with modulation doping in terms of a finite element formulation. The finite element approach corresponds to the discretization of a functional integral over the Lagrangian density defined as the functional to be made stationary. The variational principle is invoked after the discretization of the functional is performed and the spatial dependence is integrated out. The same method is applied to both the Schrödinger and Poisson functionals. While the total functional is the sum of the Schrödinger and the Poisson parts, we vary the total functional independently with respect to the Schrödinger wavefunction and also by the electrostatic potential to obtain two coupled equations. Poisson's equation is nonlinear in the change in the potential, and the nonlinearity is accounted for by iterating over a locally linearized form. An added complication is that the electronic portion of the charge density requires the calculation of the wavefunctions for *all* in-plane wave vectors (a matrix diagonalization), which is a very time-consuming calculation. These wavefunctions are dependent on the in-plane dispersion and should be taken into account even for a one-band calculation.

Given the nonlinear nature of the calculation we separate it into two nested loops. In the outer iteration loop, the electronic charge density is calculated and updated by solving Schrödinger's equation with the latest value of the potential energy. In the inner loop, the ionized donor charge is evaluated together with the *local* feedback to the electronic charge density. Both the donor and the mobile charge densities act as source terms in the Poisson equation which is solved to obtain the change in the potential energy through the given inner iteration loop. Typically, the number of (fast) iterations in the inner loop can be $10 \sim 100$ for each outer loop, and overall convergence is achieved in $5 \sim 20$ outer loop (slower) iterations. This break-up into nested iteration loops was also advocated by Trellakis, *et al.*[10]

Throughout the calculations we take advantage of the finite element representation of the discretized integrals for the Schrödinger and Poisson functionals. Most of the global

matrices are calculated only once in the finite element framework – an advantage in the large matrix analysis used in this iterative approach. The matrices are banded and sparse and we exploit this in our matrix computation algorithms. We also have of quadratic convergence to the minimum, in the variational sense, in the finite element approach. By using a Taylor expansion through the lowest order, *functional derivatives* are evaluated through the variation of the nodal values of the discretized functions. This too provides numerical simplifications within the finite element framework, while representing a general way of implementing functional derivatives numerically, since the values of the discretized functions at the nodes alone determine them; the interpolation polynomials are not altered.

The essential theory for obtaining electronic wavefunctions in the FEM is derived in section II. We describe, very briefly, the use of FEM for the determination of bound state eigenvalues and wavefunctions and for the scattering states. The algorithm for the solution of Poisson's equation is presented in section III. Examples of selfconsistent calculations for III-V layered heterostructures are presented in section IV.

2. SCHRÖDINGER'S EQUATION

2.1. A finite element formulation

We begin by considering Schrödinger's equation in the layered quantum heterostructure for a conduction band electron using the spherical effective mass approximation.[11] An extension to the multiband representation of the electronic states is straightforward and this is used in the example calculations that follow. The envelope functions satisfy the equation

$$-\frac{\hbar^2}{2}\nabla\left(\frac{1}{m^*(z)}\,\nabla\psi(\mathbf{r})\right)+V(z)\,\psi(\mathbf{r})=E\,\psi(\mathbf{r}). \tag{1}$$

Here, $\psi(\mathbf{r})$ represents the wave function in the structure, where each layer is for the moment assumed to have a uniform composition and a constant effective mass. The potential energy $V(z)$ is the superposition of the potential energy due to the conduction band offsets at interfaces between layers, which may be denoted by $V_0(z)$, and $V^{ch}(z)$, which arises from the presence of ionized donors and the free charges released by them, so that

$$V(z)=V_0(z)+V^{ch}(z). \tag{2}$$

The changes in the potential function due to charge redistribution can be substantial, as shown in Fig. 1.

We further assume that the electron is free in the in-plane direction, so that the envelope portion of the three-dimensional wavefunction in the effective mass approximation takes the form

$$\psi(r)=\frac{1}{L}\,e^{ik_x x}e^{ik_y y}f(z), \tag{3}$$

where L is an in-plane quantization length. Substituting Eq. (3) into Eq. (1) we obtain an equation for $f(z)$ in any given layer given by

$$-\frac{\hbar^2}{2m^*}\frac{d^2}{dz^2}f(z,k_\|)+\frac{\hbar^2k_\|^2}{2m^*}f(z,k_\|)$$

$$+V(z)f(z,k_\|)=Ef(z,k_\|), \tag{4}$$

whose solution for the composite heterostructure gives us the envelope functions and the energy eigenvalues of the quantum system. Here $\mathbf{k}_\|=(k_x,\,k_y)$ represents the in-plane wave vector.

The action integral is defined by

$$\mathbf{A}[f^*, f] = \int dt\, \mathcal{A} = \int dt \int dz\, \mathcal{L}(f^*, f),$$

and

$$\mathcal{A} = \int dz f^*(z) \left[\frac{\overleftarrow{d}}{dz} \frac{\hbar^2}{2m^*} \frac{\overrightarrow{d}}{dz} + \frac{\hbar^2 k_\parallel^2}{2m^*} + V(z) - E \right] f(z), \tag{5}$$

from which we can derive Schrödinger's equation, Eq. (1), using the principle of stationary action. Here the Lagrangian density $\mathcal{L}$ has no explicit time dependence. We start by discretizing the physical region into *elements*, line segments in the one-dimensional case, with special points called *nodes* that include the endpoints. In each element, the z-dependent part of the envelope wave function, $f(z)$, is represented as the sum of its as-yet-unknown value at each node multiplied by a Lagrange interpolation polynomial, called a shape function $N_\alpha(z)$. Each shape function is nonzero only in the particular elements containing or sharing the node α, and satisfies the relation $N_\alpha(z_\beta) = \delta_{\alpha\beta}$, where z_β is the location of node β. These properties allow $f(z)$ to be expressed at any coordinate in the system as

$$f(z) = \sum_\alpha N_\alpha(z) f(z_\alpha), \tag{6}$$

with index α referring to the node number for the global system. If additional accuracy is desired, two degrees of freedom are used at each node by considering both $f(z_\alpha)$ and $f'(z_\alpha)$ to be nodal variables that are multiplied by Hermite interpolation polynomials for shape functions.[12] We then decompose $f(z)$ in the form

$$f(z) = \sum_\alpha N_\alpha(z) \phi_\alpha, \tag{7}$$

where the array elements of ϕ_α alternate between the value of the function at the node and the value of the derivative of function at the same node.

We substitute Eq. (7) into Eq. (5) and integrate out the known spatial dependence over each element. The functional integral in element *iel* is given by

$$\mathcal{A}^{iel}[f^*, f] = \phi_\alpha^* [A_{\alpha\beta}^{(iel)} + B_{\alpha\beta}^{(iel)} - E\, S_{\alpha\beta}^{(iel)}] \phi_\beta, \tag{8}$$

with $A^{(iel)}$ containing the kinetic energy contribution, $B^{(iel)}$ having the potential energy contributions, and $S^{(iel)}$ being the wavefunction overlap matrix. These contributions are added

up to obtain the discretized form of the total functional. The individual element matrices $A^{(iel)}$, $B^{(iel)}$, and $S^{(iel)}$ are inserted into the corresponding global matrices. Appropriate care is taken to overlay the element matrices to ensure that inter-element continuity is enforced at the shared node between two elements. The resulting functional integral is given by

$$\mathcal{A}[f^*, f] \;=\; \phi^*_\alpha [A_{\alpha\beta} + B_{\alpha\beta} - E\, S_{\alpha\beta}] \phi_\beta. \tag{9}$$

We now invoke the (nodal) variational principle to obtain

$$\frac{\delta \mathcal{A}}{\delta \phi^*_\alpha} \;=\; 0, \tag{10}$$

or

$$(A_{\alpha\beta} + B_{\alpha\beta})\, \phi_\beta = E\, S_{\alpha\beta}\, \phi_\beta, \tag{11}$$

which is the discretized Schrödinger equation represented here as a generalized eigenvalue problem, with eigenvectors ϕ having the nodal values and nodal derivatives of $f(z)$ as components. Here the overlap matrix $S_{\alpha\beta}$ is not diagonal because the shape functions are not orthogonal. In practice, the matrix $A_{\alpha\beta}$ is separated into terms dependent on powers of k_x and k_y. In the 1-band case

$$\begin{aligned} A_{\alpha\beta} \;&=\; \sum_{iel} A^{iel}[f^*, f] \\ &=\; A^{(0)}_{\alpha\beta} + k_x^2 A^{(1)}_{\alpha\beta} + k_y^2 A^{(2)}_{\alpha\beta}. \end{aligned} \tag{12}$$

Then the global matrices $A^{(0)}$, $A^{(1)}$ and $A^{(2)}$ are not recalculated for each value of k_x, k_y, but rather are stored in memory so that the reconstruction of A in Eq. (12) is very rapid. This has the added advantage that we can immediately apply the Feynman-Hellmann theorem[13] to obtain the in-plane effective mass of the carrier in the system. Given the solution of the eigenvalue problem, Eq. (11), and the corresponding eigenfunctions ϕ^i_β, the effective mass in the ith energy subband level is given by

$$\begin{aligned} \frac{1}{m^*_i} \;&=\; \frac{1}{\hbar^2} \left\langle f_i \,\middle|\, \frac{\partial^2 H}{\partial k_x^2} \,\middle|\, f_i \right\rangle, \\ &=\; \frac{2}{\hbar^2}\, \phi^i_\alpha\; A^{(1)}_{\alpha\beta}\, \phi^i_\beta. \end{aligned} \tag{13}$$

Again, the overlap matrix $S_{\alpha\beta}$ is computed only once. The matrix $B_{\alpha\beta}$ contains the potential energy term, and this is reevaluated as the potential energy function is updated in the iterations.

With 3∼10 quintic Hermite elements per layer, the matrix dimensions are typically 250∼2500 with a bandwidth of 6 (diagonal + supradiagonal) leading to fairly sparse matrices.

2.2. Boundary and interface conditions in the FEM

For any layered semiconductor structure at hand, we now apply boundary conditions to the wavefunctions at the left and right ends of the heterostructure by specifying the values of the wavefunction or its derivative at the initial and final nodes. The boundary nodal values depend on whether we are considering bound states, free (traveling) states, or quasibound states.

For bound states, the wavefunction is zero at the left and right boundaries, far into the barrier regions. These boundary conditions are now built into the set of simultaneous equations, Eq. (11).[14]

For free and quasibound states we have to account for the form of incoming and outgoing traveling waves. While the finite element approach gives the total wavefunction, we are concerned with boundary conditions on the incoming or outgoing wave amplitudes. This calls for a modal analysis of the wavefunction in terms of the incoming and outgoing component wavefunctions at the two ends. For such scattering problems, the energy E of the incident wave is given. We rewrite Eq. (5) to include additional surface terms needed to express the conditions on the incoming and outgoing probability currents at z_L and z_R.

For a wave incident from the left with amplitude a we have

$$\begin{aligned} f(z_L) &= a\,e^{ik_L z_L} + r\,e^{-ik_L z_L}, \\ f'(z_L) &= ik_L(a\,e^{ik_L z_L} - r\,e^{-ik_L z_L}), \end{aligned} \tag{14}$$

where the reflected wave has amplitude r. Thus the boundary condition on the left is given by

$$f'(z_L) + ik_L\,f(z_L) = 2ik_L\,a\,e^{ik_L z_L}. \tag{15}$$

Similarly, on the right side, we have

$$f'(z_R) = ik_R\,f(z_R), \tag{16}$$

since $f(z) = t\ \exp(ik_R z)$ in this region. These two boundary conditions are incorporated into the functional by writing

$$\begin{aligned}\mathcal{A}[f^*, f] &= \int dz\, \mathcal{L}(f^*, f) \\ &= \int dz\, f^*(z)\left[\frac{\overleftarrow{d}}{dz}\frac{\hbar^2}{2m^*}\frac{\overrightarrow{d}}{dz} + \frac{\hbar^2 k_\parallel^2}{2m^*} + V(z) - E\right] f(z) \\ &\qquad -ik_R\, f^*(z) f(z)\Big|_{z_R} \\ &\qquad -f^*(z)[ik_L\, f(z) - 2i\, k_L a e^{ik_L z}]\Big|_{z_L}\ . \end{aligned} \tag{17}$$

The variational principle now gives Schrödinger's equation and also the mixed boundary conditions of Eq. (14) required of scattering states above the barriers. The discretization of the functional integral leads to global matrices analogous to the case of bound states except that now we have at hand a set of simultaneous equations with driving terms proportional to the incident amplitude a taken over to the right side.

In addition to the boundary conditions at the endpoints, we have to ensure the continuity of the wave function and of the probability current across interfaces between the layers in the heterostructure. This is implemented by the continuity of ψ'/m^* across interfaces. For the case of one degree of freedom per node, the continuity of the probability current is implicitly built in, while for two degrees of freedom per node, the element matrices need to be modified before they are overlaid to form the global matrices. For the element just to the right of the interface we replace its right nodal derivative evaluated at the interface nodal location with $\phi'_R(z) = (m^*_R/m^*_L)\phi'_L(z)$. We can apply the interface constraint by multiplying the row and column of the element matrix iel_R appropriately by the effective mass ratio before overlaying onto the global matrix.

The bound state wavefunction is normalized such that $\int_{-\infty}^{\infty} dz|f(z)|^2 = 1$, as usual. The free state wavefuntion is normalized such that the incoming wave has an amplitude of $\frac{1}{\sqrt{2\pi}}$.[15] Now $\int_{\Omega_k} dk \int_{\Omega} dz|f(z)|^2$ is the number of states in the phase space $\Omega_k\Omega$. Alternatively, we can set the amplitude of the incoming wave to be 1 and use $\int_{\Omega_k} \frac{dk}{2\pi} \int_{\Omega} dz|f(z)|^2$ to calculate the number of states. Under these normalization conditions, $|f(z)|^2$ for a bound state has a dimension of inverse length, but is dimensionless for a free state. In Fig. 2 we show the lowest two heavy hole wavefunctions of the single quantum well of Fig. 1.

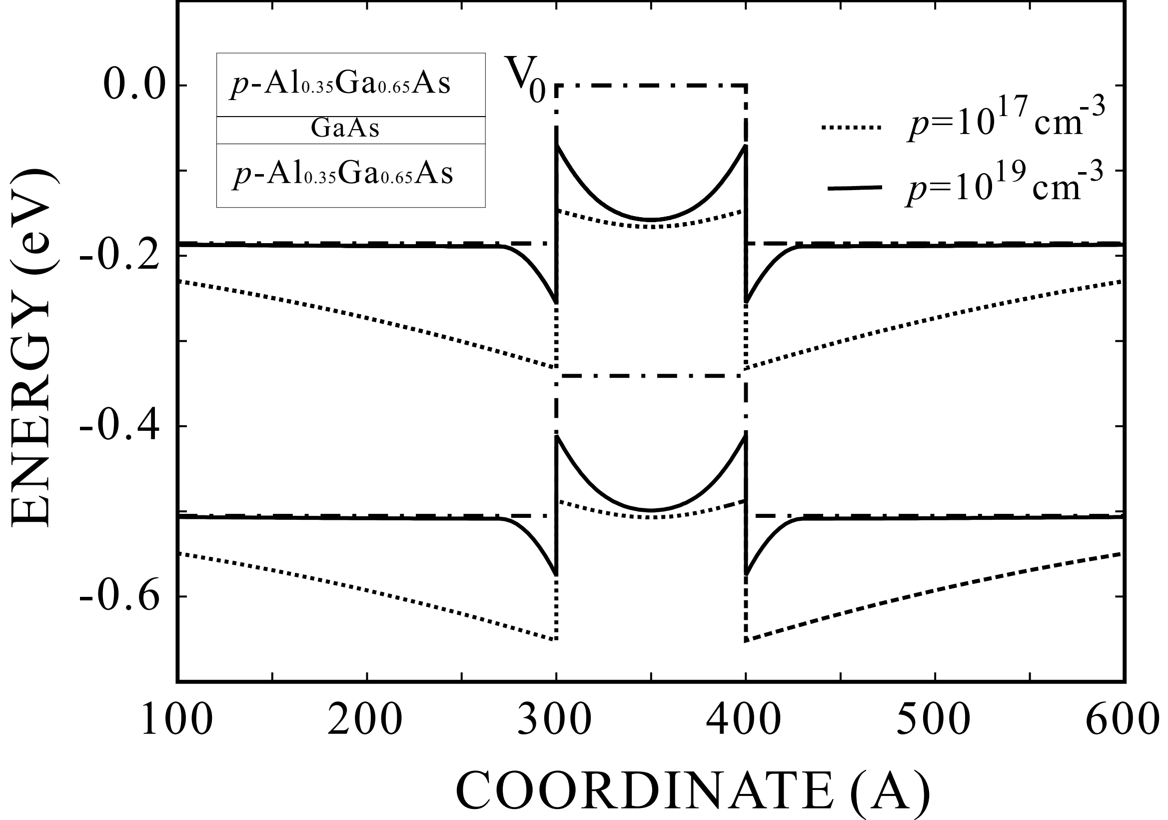

FIG. 1: The bending of the valence band edge in a 100 Å GaAs quantum well with $Ga_{0.65}Al_{0.35}As$ barriers that are p-doped (i) to 1.0×10^{17} cm^{-3} (dotted line), and (ii) to 1.0×10^{19} cm^{-3} (solid line), are shown. The dot-dashed line marked by V_0 is the potential due to band offsets before band bending. Note the larger depletion region generated in the case of lower doping.

3. POISSON'S EQUATION

Now consider the Poisson equation in the selfconsistent problem.[16] It is useful to multiply the potential function by $-|e|$, the electronic unit of charge, so that we directly solve for the potential energy $V^{ch}(z)$. We begin with the Poisson functional $\mathcal{P}$

$$\mathcal{P}[V] \; = \; \int dz \Bigg[\frac{1}{2} \left(\frac{d\, V^{ch}(z)}{dz} \right) \epsilon(z) \left(\frac{d\, V^{ch}(z)}{dz} \right) + 4\pi |e| \Bigg(\rho_d(V(z)) + \rho_n(V(z)) \Bigg) V^{ch}(z) \Bigg], \tag{18}$$

where ϵ is the dielectric function assumed to be constant in each layer, ρ is the charge density which is a function of the total potential, and the subscripts d and n refer to the ionized donor and the free electron charge densities, respectively. The potential arising from

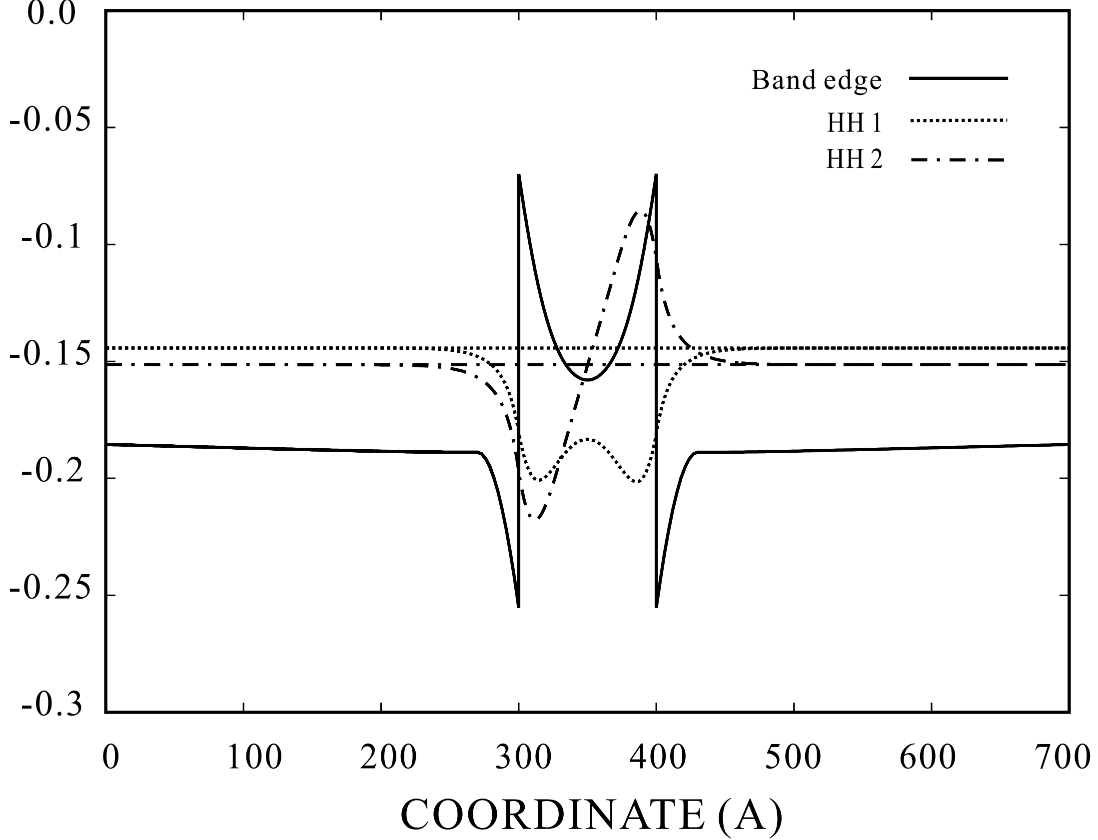

FIG. 2: The lowest two heavy hole wavefunctions and their energy eigenvalues (horizontal lines) in a 100 Å GaAs quantum well with $Ga_{0.65}Al_{0.35}As$ barriers that are p-doped to 1.0×10^{19} cm^{-3} (Fig. 1) are shown. The wavefunctions and the band edge have been labeled in the legend. Note the wavefunctions which reflect the double-well nature of the quantum well under selfconsistent band bending.

the band offsets at the heterointerfaces, and the potential arising from the spatially varying charge densities ρ_n and ρ_d, all contribute to the total potential $V(z)$. Now $\mathcal{P}$ is discretized using finite elements and is minimized with respect to $V^{ch}(z)$.

3.1. The source terms

The second term in the integrand in Eq. (18) is the ionized donor contribution to the charge density, which determines the depletion regions. At zero temperature, the donor charge density is $\rho_d(z) = e\,n_d(z)\,\theta(V(z) - E_d - E_F)$, where $\theta(x)$ is the Heaviside step function, $n_d(z)$ is the number density of the donors, $V(z)$ is the total potential, E_d is the binding energy of the donors, and E_F is the quasi-Fermi level. At finite temperature, the

donor charge density is

$$\rho_d(z) = \frac{|e|\, n_d(z)}{1 + 2\, \exp[(E_F + E_d - V(z))/k_B T]}, \tag{19}$$

where T is the temperature.

The third term in the integrand in Eq. (18) is the free-carrier electronic charge density and is given by

$$\rho_n(z) = -2|e| \sum\!\!\!\!\!\!\int_\nu \int \frac{d^2 k_\parallel}{(2\pi)^2} \, |f_\nu(z, k_\parallel)|^2 \times \mathcal{F}(E_\nu(k_\parallel), E_F, T), \tag{20}$$

where the symbol $\sum\!\!\!\!\!\!\int$ succinctly represents the sum over discrete bound states and an integral over the continuum states, labeled by ν, associated with the energy for the motion along z. Here $f_\nu(z, k_\parallel)$ is the z component of the envelope portion of the wavefunction and $\mathcal{F}$ is the Fermi function. The wavefuntion, $f_\nu(z, k_\parallel)$ and its corresponding energies, $E_\nu(k_\parallel)$, are found by solution to the Schrödinger equation for each value of the integration variable, $k_\parallel$. We step in the integration variable, $k_\parallel$, until the additional charge becomes negligible.

Converting the integral in Eq. (20) directly into an integral over the density-of-states (DOS) multiplied by the Fermi factor may not be simple in general, since the dispersion relation in energy can be nonparabolic for bound states in a heterostructure. This is certainly the case for the complex valence band structure of heterostructures; it is also the case even within the simple one band effective mass model. A simple way of evaluating this integral is to consider a series of energy intervals or bins of width 1∼5 meV. The energy spectrum is given in terms of $\{\nu,\, k_\parallel\}$ and the corresponding wavefunctions are known. Then the integral is evaluated in discrete cells in momentum space and stored in the corresponding energy bins. We label the DOS in the energy bin i at E_i as $\Lambda_i(z)$. The Fermi function weights the partial contributions of the integral in the various bins, and the sum is the total charge density. By staying in momentum space, and using the energy discretization, we evaluate the DOS directly. We thus have at hand the charge density in the form

$$\rho_n(z) = -|e| \sum_i \Lambda_i(z)\, \mathcal{F}(E_i, E_F, T), \tag{21}$$

with the accuracy depending on the level of discretization. Earlier approaches[17–20] to the evaluation of the DOS in semiconductors exploit the known energy dispersion curves over a

grid of points and employ interpolation in order to perform the integrals. The determination of the Jacobian of transformation from momentum integrals to an integral over energy entails the gradient of the energy dispersion in the denominator. This requires additional care in order to evaluate it accurately. The crossing of the energy dispersion surfaces across given energy planes is required in order to obtain the energy gradients in these methods. The method used in this thesis is effective enough for the in-plane 2D phase space evaluations essential to layered semiconductors. Improving the accuracy of the DOS calculation would require us to reduce the size of the energy bins, leading to increasing time for the computation. It is clear that this issue should be revisited in order to develop a fast and numerically accurate approach to the evaluation of the DOS.

The Fermi level is determined as follows. For the modulation doped quantum wells in which the barrier can supply enough carriers to fill the well up to Fermi level, the Fermi level for the whole heterostructure can be taken to be the Fermi level in the bulk region on either end of the heterostructure. The bulk Fermi level must be calculated using the donor and electronic charge densities. We use

$$\rho_D(z, E_f, E_D) + \rho_{n,bulk}(z, E_F) = 0 \tag{22}$$

to determine the Fermi level through a root finding procedure.[21] The electronic charge density in the bulk is given at T=0 K by

$$\rho_{n,bulk} = -|e|(2m^*(E_F - E_c)/\hbar^2)^{3/2}/3\pi^2, \tag{23}$$

E_c being the conduction band edge energy, and at finite temperature we have

$$\begin{aligned}\rho_{n,\,bulk} &= -\frac{|e|}{2\pi^2}\left(\frac{2m^* k_B T}{\hbar^2}\right)^{3/2} \\ &\times \int_0^\infty d\xi \,\ln\left[1 + e^{-\xi^2}\, e^{(E_F - E_c)/k_B T}\right].\end{aligned} \tag{24}$$

The conduction band edge is assumed to be at E_c in the above expression.

If the doped barrier in a superlattice is not thick enough to supply the needed carriers, or if the well is doped, there is no easy way to predict the location of the Fermi level. In this case, the Fermi level should be found by assuming a trial Fermi level and monitoring the slope of the potential in the barrier region in the case of quantum well or watching the continuity of the slope of the potential at the interface between one period and the next period in the case of superlattice.

The solution of Eq. (18) entails using the charge distributions as source terms which in turn depend on the potential energy. The method of solution is given below.

3.2. Selfconsistency iterations

The charge density is nonlinear in $V(z)$ and is linearized in each element so that the final solution may be approached iteratively starting from an initial guess for the potential energy. An overview of the method is now in order.

We have two parts to the problem. The first is a time-consuming diagonalization of the Schrödinger equation for bound states, and solving for the wavefunctions for each free or quasibound state as well, using the latest potential obtained through iteration. The resulting wavefunctions are used to calculate ρ_n. The second part is the solution of the Poisson's equation for the change in the potential energy. This requires the calculation of the ionized donor charge density. This inner loop can be iterated over quickly with corresponding small corrections to the carrier densities estimated to first order. While this is a faster calculation the ionized donor density can be a discontinuous function. Invoking superposition, we evaluate only the *changes* in the potential energy due to changes in the charges as estimates for both ρ_n and ρ_d are updated in the inner loop iterations. Once this calculation has stabilized, we return to the slower calculation for updating solutions to Schrödinger's equation.

We now provide the notational details. Start with an initial guess for the potential energy: $V^{ch}_{j=0,\,k=0}(z)$. Here the indices j and k refer to the outer and inner loops, respectively. The function $V^{ch}_{j=0,\,k=0}(z)$ can be selected as follows. We require this potential to be zero at the edges of the layered structure under consideration where the asymptotic values of $V_0(z)$ prevail. In the absence of an external field we also require that $V^{ch}_{0,\,0}(z)$ have zero derivatives at the edges.[6, 22] An initial guess of a cubic function is adequate for our purposes to account for any mismatch in the value of V_0 at the two ends. In practice, these boundary conditions will have to be modified if the modeled system is truncated and does not extend far enough into bulk regions.

For the jth iteration of the Schrödinger solver we use the updated potential energy $V_{j,\,0}(z)$, and determine the charge density $\rho_n(V^{ch}_{j,\,0})$. The inner loop is then initiated starting with the index $k = 0$. In each inner loop iteration we evaluate the Poisson functional integral

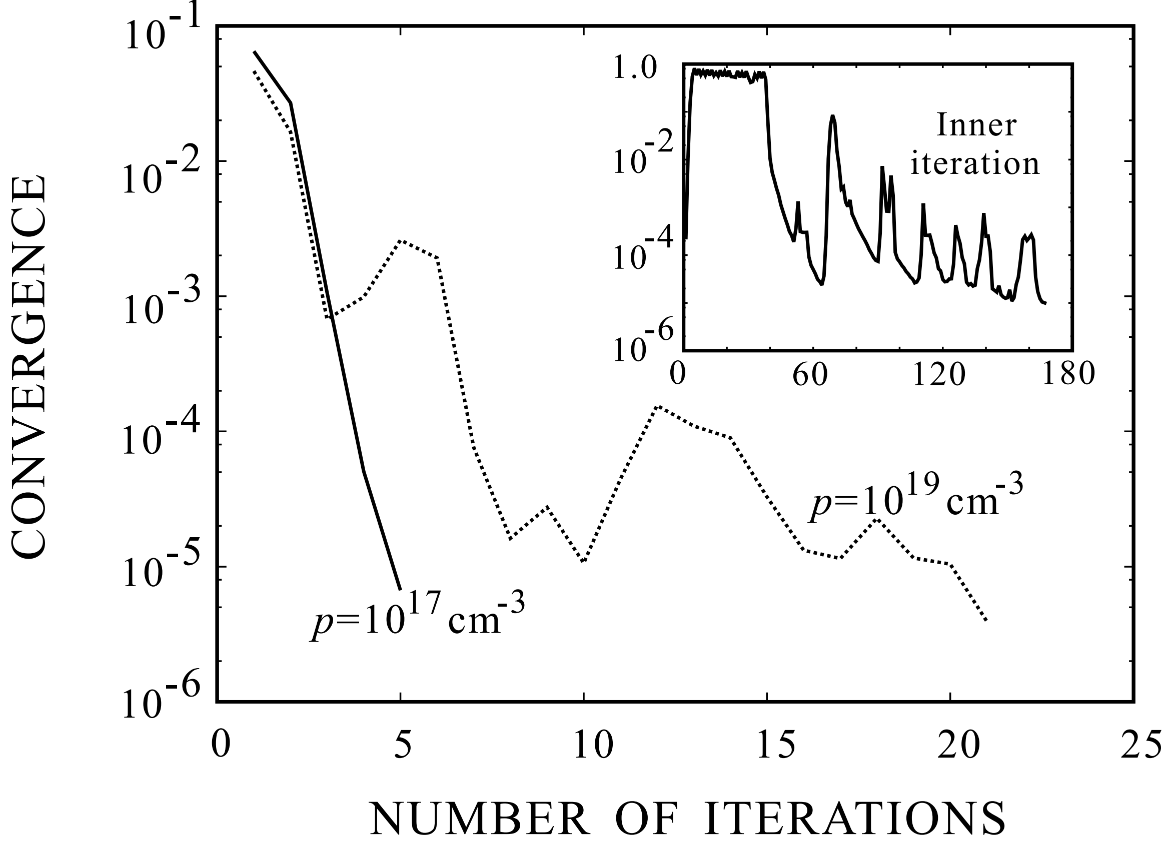

FIG. 3: The rate of convergence for the potential function of the p-doped quantum well of Fig. 1 versus the number of outer (Schrödinger) iterations is shown. For a p-doping level of 1×10^{17} cm^{-3} convergence to 1×10^{-5} eV is achieved in 5 iterations, and for p-doping of 1×10^{19} cm^{-3} convergence is achieved in 21 iterations. A typical rate of convergence in the inner (Poisson) iteration is shown in the inset.

$\mathcal{P}$ minimizing it with respect to the nodal values of the potential. The resulting Poisson's equation is solved by successively working with the discretized form. Here, we solve for just the change $\delta V^{ch}_{j,k}$ in the potential energy at the $(j,k)^{th}$ iteration defined by

$$V^{ch}_{j,k+1} = V^{ch}_{j,k} + \delta V^{ch}_{j,k}. \tag{25}$$

We use a scaling factor λ in order to dampen oscillations in the iterative process. Here λ is a control parameter, $0 < \lambda \leq 1$, that is adjusted to accelerate convergence in the inner loop. If the changes in the charges oscillate over two consecutive iterations, λ is lowered so that a more conservative change in the potential energy is accepted. The convergence criterion for the inner loop can be numerically quantified by evaluating the vector 1-norm of the difference between the nodal values at the nodes β only, rather than integrating the

modulus of the difference between these functions.

$$\frac{1}{N_g}\sum_{\beta}^{N_g}|V^{ch,\,\beta}_{j,\,k_{max}} - V^{ch,\,\beta}_{j,\,k_{max}-1}| < \eta_1, \tag{26}$$

where N_g is the array size of the vectors and $\eta_1 \sim 10^{-5}$, say. The parameter λ is reset to unity for each k-loop. In the initial iterations of the inner loop the change in potential δV^{ch} can be significant enough to demand the use of λ; however, as we proceed through these iterations we are solving for smaller and smaller quantities δV^{ch} and hence the role of λ becomes less important. The need for such damping factors is well appreciated in the literature.[6, 23, 24] An example of the rate of convergence with the number of iterations is displayed in Fig. 3. The number of iterations to convergence to 1.0×10^{-5} eV in the change in the potential function is shown for a p-doped quantum well of Fig. 1.

Assume that we are given the final output of the inner loop as $V^{ch}_{j,k_{max}}(z)$. We re-initiate the outer loop calculation with $j \to j+1$ and $k_{max} \to 0$ and iterate until charge neutrality is achieved. Equivalently, we require that the potential energy $V^{ch}_{j+1,\,0}(z)$ has not changed substantially from the $V^{ch}_{j,\,0}(z)$ within a tolerance $\eta_2 \sim 10^{-5}$ over the entire structure. For convergence we require

$$\frac{1}{N_g}\sum_{\beta}^{N_g}|V^{ch,\,\beta}_{j+1,\,0} - V^{ch,\,\beta}_{j,\,0}| < \eta_2. \tag{27}$$

On convergence, charge neutrality occurs naturally in the modeled structure extended far enough to be represented by bulk regions at the ends. Charge neutrality may not be a valid criterion if the structure is truncated before the depletion region is included in the modeled structure. However, we can still reach convergence in V^{ch} with a truncated physical region if the potential energies at the two ends are specified. Here again we may include a damping factor μ to control the fraction of δV that is included in $V^{ch}_{j+1,\,0}$. The outer iteration is stopped when the tolerance criterion, Eq. (27), is satisfied.

3.3. Finite element implementation

At the $(j,k)^{th}$ iteration, the Poisson functional $\mathcal{P}$ can be written in terms of

$$V^{ch}(z) \;=\; V^{ch}_{j,\,k}(z) + \delta V^{ch}_{j,\,k}(z). \tag{28}$$

This scalar potential is expressed in each finite element in terms of interpolation shape functions in the form

$$V^{ch}(z) = \sum_{\alpha} V^{ch}_{\alpha} N_{\alpha}(z), \tag{29}$$

and is substituted into Eq. (18). In the following, we suppress the dependence of ρ_n and ρ_d on the band offset potential V_0. Let us represent the change in the carrier charge density as the potential energy changes from $V^{ch}_{j,0}$ to $V^{ch}_{j,k}$ by

$$\Delta\rho_n(V^{ch}_{j,k} + \delta V^{ch}_{j,k}) = \rho_n(V^{ch}_{j,k} + \delta V^{ch}_{j,k}) - \rho_n(V^{ch}_{j,0}). \tag{30}$$

This can be approximated as follows. As in Eq. (21), we discretize the integrations in Eq. (20) over $\{\nu, k_{\parallel}\}$ into bins in the electronic total energy. Using the same DOS factors but altering the Fermi distribution function alone, we write

$$\begin{aligned}\Delta\rho_n(V^{ch}_{j,k} + \delta V^{ch}_{j,k}) &= \\ \sum_i \Lambda_i(z) \big[\mathcal{F}(E_i + V^{ch}_{j,k} + \delta V^{ch}_{j,k} - V^{ch}_{j,0}, E_F, T) \\ - \mathcal{F}(E_i, E_F, T) \big] .\end{aligned} \tag{31}$$

In other words, instead of updating E_i all over again by employing the Schrödinger solver, we account for the change in energy appearing in the Fermi function by adding the change in the potential energy to E_i.[10] The above expression is consistent with the condition $\Delta\rho_n(V^{ch}_{j,0}) = 0$, since for $k = 0$ we have already determined $\rho_n(V^{ch}_{j,0})$.

Substituting Eqs. (28-31) in Eq. (18), and using the expression $V_{j,k+1,\alpha} = V_{j,k,\alpha} + \delta V_{j,k,\alpha}$, we obtain

$$\begin{aligned}\mathcal{P} \;=\; & V_{j,k+1,\alpha} \frac{1}{2} \int dz \left(N'_{\alpha}(z) \epsilon(z) N'_{\beta}(z) \right) V_{j,k+1,\beta} \\ & + V_{j,k+1,\alpha}\, 4\pi|e| \int dz\, N_{\alpha}(z)\, \rho_d(V^{ch}_{j,k}(z) + \delta V^{ch}_{j,k}(z)) \\ & + V_{j,k+1,\alpha}\; 4\pi|e| \int dz\, N_{\alpha}(z) \Big(\rho_n(V^{ch}_{j,0}) \\ & \qquad + \Delta\rho_n(V^{ch}_{j,k} + \delta V^{ch}_{j,k}) \Big).\end{aligned} \tag{32}$$

We now write the integrals in Eq. (32) using a matrix notation. Define

$$M_{\alpha\beta} = \int dz\, N'_{\alpha}(z)\, \epsilon(z)\, N'_{\beta}(z). \tag{33}$$

The matrix $M_{\alpha\beta}$ is evaluated once and systematically reused in the iterations. While all the charge densities appearing in the integrals on the right side of Eq. (32) are not known, we can formally write the integrals as vector arrays with the spatial dependence integrated out.

Let us consider these integrals one by one.

(i) With $V_{j,\,k}(z)$ expressed in terms of the interpolation polynomials in each finite element, the integral over the donor charge density can be written as

$$4\pi|e|\int dz N_\alpha(z)\rho_d(V_{j,\,k}(z)+\delta V_{j,\,k}(z)) \equiv G_\alpha(\{V^{ch}_{j,\,k,\,\beta}+\delta V^{ch}_{j,\,k,\,\beta}\}), \tag{34}$$

where the *set* of variables $\{V^{ch}_{j,\,k,\,\beta}+\delta V^{ch}_{j,\,k,\,\beta}\}$ refer to the nodal values of the potential energy functions at the nodes β. A Taylor expansion of the charge density $\rho_d(V(z),z)$ with respect to $V(z)=(V_0(z)+V^{ch}(z)+\delta V^{ch}(z))$ entails a functional differentiation that is obviously nontrivial to evaluate. However, we can approximate $G_\alpha(\{V^{ch}_{j,\,k,\,\beta}+\delta V^{ch}_{j,\,k,\,\beta}\})$ by

$$\begin{aligned} G_\alpha(\{V^{ch}_{j,\,k,\,\beta}+\delta V^{ch}_{j,\,k,\,\beta}\}) &= G^0_\alpha(\{V^{ch}_{j,\,k,\,\beta}\})+\sum_\beta \frac{\partial G_\alpha}{\partial V^{ch}_{j,\,k,\,\beta}}\cdot\delta V^{ch}_{j,\,k,\,\beta}, \\ &= G^0_\alpha+\sum_\beta G^1_{\alpha\beta}\cdot\delta V^{ch}_{j,\,k,\,\beta} \end{aligned} \tag{35}$$

where $G^1_{\alpha\beta}$ in the second term is represented by

$$G^1_{\alpha\beta}=4\pi|e|\int dz N_\alpha(z)\left[\frac{\rho_d(V^{ch}_{j,k}(z)+[V^{ch}_{j,k,\beta}-V^{ch}_{j,k-1,\beta}])-\rho_d(V^{ch}_{j,k}(z)-[V^{ch}_{j,k,\beta}-V^{ch}_{j,k-1,\beta}])}{2(V^{ch}_{j,\,k,\,\beta}-V^{ch}_{j,\,k-1,\,\beta})}\right]. \tag{36}$$

Here $V^{ch}_{j,\,k}(z)$ and $V^{ch}_{j,\,k-1}(z)$ are known at every z, except in the $k=0$ case, and ρ_d in the above expression is a known function. (For $k=0$, this derivative is not evaluated.) The incremental difference $V^{ch}_{j,\,k,\,\beta}-V^{ch}_{j,\,k-1,\,\beta}$ in the nodal values corresponds to the change in one iteration of the inner loop and is a known, small quantity. In effect, we have approximated the functional derivative of $\rho_d(z)$ with respect to the potential energy function $V^{ch}(z)$ by the derivative with respect to the variations in the nodal variables representing V. This discretized version of the derivative may be justified by noting that the only variations that are allowed in the interpolated form of the potential energy function are the nodal values of the potential

energy. Each nodal value is independently varied in order to approximate the functional variation of V^{ch} at every coordinate. Here $G^{1}_{\alpha\,\beta}$ is block-diagonal and again expressible in a sparse matrix format. (While ρ_d can be evaluated analytically, it varies abruptly with z and its derivative becomes a highly peaked function. The numerical differentiation effectively smoothes out the result and is easier to represent in computation.)

(ii) The third term on the right side of Eq. (32) is

$$J_\alpha = 4\pi|e| \int dz\, N_\alpha(z)\, \rho_n(V^{ch}_{j,0}(z)). \tag{37}$$

Here $\rho_n(V^{ch}_{j,0}(z))$ is explicitly determined during the outer loop as soon as one steps out of the inner loop. The carrier charge density is given by Eq. (20), in which all the factors are known.

(iii) The last term in Eq. (32) is

$$\begin{aligned} 4\pi|e| \int dz\, N_\alpha(z)\, &\left[\Delta\rho_n(V^{ch}_{j,k} + \delta V^{ch}_{j,k})\right] \\ &= K_\alpha(\{V^{ch}_{j,k,\beta} + \delta V^{ch}_{j,k,\beta}\}) \\ &= K^0_\alpha + \sum_\beta \frac{\partial K_\alpha}{\partial V^{ch}_{j,k,\beta}} \cdot \delta V^{ch}_{j,k,\beta} \\ &= K^0_\alpha + \sum_\beta K^1_{\alpha\beta} \cdot \delta V^{ch}_{j,k,\beta}. \end{aligned} \tag{38}$$

The first term, K^0_α is readily evaluated numerically in the $(j,\, k)^{th}$ iteration using Eq. (31) to obtain

$$\begin{aligned} K^0_\alpha = 4\pi|e| \int dz\, N_\alpha(z) \sum_i \Lambda_i(z) \times \\ \Big(\mathcal{F}(E_i + V^{ch}_{j,k}(z) - V^{ch}_{j,0}(z), E_F, T) - \mathcal{F}(E_i, E_F, T)\Big). \end{aligned} \tag{39}$$

We again approximate the functional derivative required in a Taylor expansion of $K_\alpha(V^{ch}(z) + \delta V^{ch}(z), z)$ by its discretized version, $\partial K_\alpha / \partial V^{ch}_{j,k\,\beta}$. Defining

$$\xi_i = E_i + V^{ch}_{j,k}(z) - V^{ch}_{j,0}(z), \tag{40}$$

we write

$$\begin{aligned} K^1_{\alpha\beta} = 4\pi|e| \int dz\, N_\alpha(z) \sum_i \Lambda_i(z) \times \\ \left(\frac{\partial \mathcal{F}(\xi_i)}{\partial \xi_i}\right) \left(\frac{\partial \xi_i}{\partial V^{ch}_{j,k,\beta}}\right). \end{aligned} \tag{41}$$

The derivatives are discretized and evaluated using

$$\frac{\partial \mathcal{F}(\xi_i)}{\partial \xi_i} = \frac{\mathcal{F}(E_{i+1} + V^{ch}_{j,k}(z) - V^{ch}_{j,0}(z)) - \mathcal{F}(E_i + V^{ch}_{j,k}(z) - V^{ch}_{j,0}(z))}{E_{i+1} - E_i}, \tag{42}$$

and

$$\begin{aligned} \frac{\partial \xi_i}{\partial V^{ch}_{j,k,\beta}} &= \frac{\partial}{\partial V^{ch}_{j,k,\beta}} \left(E_i + V^{ch}_{j,k}(z) - V^{ch}_{j,0}(z) \right) \\ &= \frac{\partial V^{ch}_{j,k}}{\partial V^{ch}_{j,k,\beta}} = N_\beta(z), \end{aligned} \tag{43}$$

so that we can evaluate the integral $K^1_{\alpha\beta}$ numerically.

Combining and rearranging all the terms in Eq. (32) the Poisson functional is given by

$$\begin{aligned} \mathcal{P}_{j,k} &= \frac{1}{2} V_{j,k+1,\alpha} \cdot M_{\alpha\beta} \cdot V_{j,k+1,\beta} \\ &\quad + V_{j,k+1,\alpha} \cdot (G^0_\alpha + J_\alpha + K^0_\alpha) \\ &\quad + V_{j,k+1,\alpha} \cdot (G^1_{\alpha\beta} + K^1_{\alpha\beta}) \cdot \delta V^{ch}_{j,k,\beta}. \end{aligned} \tag{44}$$

Invoking the variational principle for the electrostatics problem, we require $\delta \mathcal{P} / \delta V_{j,k,\alpha} = 0$, which leads to

$$\begin{aligned} &\left[M_{\alpha\beta} + G^1_{\alpha\beta} + K^1_{\alpha\beta} \right] \cdot \delta V^{ch}_{j,k,\beta} \\ &\qquad = - \left(M_{\alpha\beta} \cdot V^{ch}_{j,k,\beta} + G^0_\alpha + J_\alpha + K^0_\alpha \right). \end{aligned} \tag{45}$$

Thus at each inner loop iteration we determine the "small" change in the potential energy δV^{ch} by solving the above set of simultaneous equations.[25] The solution at nodal locations are then used to reconstruct δV everywhere.

In the above discussion, we have purposely left the details of the heterostructure unspecified. The only features it needs to have are that it is modulation-doped, the doping profile being specified by $n_d(z)$; the structure can have bound states, quasibound states, and free or traveling states. We have exploited the method of finite elements and discretized the physical region into elements in which the carrier wavefunctions and also the electrostatic potential energies are determined at nodal points. These are solved for and the complete functions reconstructed using interpolation polynomials. The method being a variational procedure, we are assured of a quadratic convergence to the minimum. By integrating out the spatial dependence we have reduced the Schrödinger-Poisson problem into one in which

we need determine only values at nodes in the elements. Functional differentiations are reduced to nodal variational derivatives. These are concrete advantages inherent in the finite element approach to this fairly complex nonlinear problem. We now present applications of this method.

4. APPLICATIONS

4.1. multi-band $\mathbf{k}\cdot\mathbf{P}$ model and selfconsistency

The approach presented in section III above for a single energy band is readily extended to a 6-band description of the valence heavy hole, light hole and spin-orbit split-off bands, and also to a full 8-band representation of the conduction and valence bands used to describe the energy band structure in typical III-V or II-VI compound semiconductors.[26] The $\mathbf{k}\cdot\mathbf{P}$ band parameters for the materials in the layers are known.[27]

The required Lagrangian has been formulated elsewhere.[28–30] While the Poisson part of the problem remains the same as in the 1-band model, the calculation of the bound, quasi-bound, and traveling states requires a careful application of boundary conditions at the two ends of a heterostructure. The boundary conditions at interfaces between the layers are also more complex.

At the interfaces, we apply the current continuity conditions for the multiband $\mathbf{k}\cdot\mathbf{P}$ model. The usual Löwdin perturbation theory[31] of degenerate bands employs the elimination of remote high energy bands in favor of the valence and the lowest conduction bands. This “folding in” of higher energy bands[32] requires additional care in the presence of layer interfaces in heterostructures.[33, 34] With the z-axis perpendicular to the layer interfaces, the functional integral takes the general form[34–36]

$$\mathcal{A} = \int dz f_i^*(z)\Big[\overleftarrow{\partial}_z(\boldsymbol{A})_{ij}\overrightarrow{\partial_z} + \overleftarrow{\partial}_z(\boldsymbol{B}_L)_{ij} + (\boldsymbol{B}_R)_{ij}\overrightarrow{\partial}_z + (\boldsymbol{C})_{ij} - E\delta_{ij}\Big] f_j(z), \tag{46}$$

where the order of the derivative terms becomes important. Here the envelope functions $f_i(z)$, $i = 1, \ldots, n_b$, have components corresponding to the number of bands n_b appearing in the $\mathbf{k}\cdot\mathbf{P}$ model that is employed. The coefficients are $n_b \times n_b$ matrices. The matrices $\mathbf{B}_L$ and $\mathbf{B}_R$ are non-Hermitian, but transform into one another under Hermitian conjugation so that the Lagrangian is Hermitian. The current continuity condition is derived from the Lagrangian through a gauge-variational approach described earlier.[30]

For bound states again we set the wavefunctions at the boundaries to zero, while for traveling states we specify the incoming plane waves. This requires a modal analysis to determine the wavevectors for given energy in the bulk-like regions at the two ends of the

heterostructure. The $\mathbf{k}\cdot\mathbf{P}$ bulk Hamiltonian

$$H\psi(\mathbf{r}) = (Ak_z^2 + i(B_R - B_L)k_z + C)\psi(\mathbf{r}) = E\psi(\mathbf{r}). \tag{47}$$

is a quadratic eigenvalue equation for k_z, given E. The plane wave eigenfunctions and wavevector-eigenvalues are determined in a straightforward manner.[37, 38] This then allows us to select the traveling wave solutions for the above-barrier states and account for them in the calculation of the carrier density; With each energy band we sum over the free carrier density by doing the finite element calculation over a discretied set of energy values. This computation is then inserted into the Poisson solver. The inclusion of strain in the layered structures generates strain related energy level splitting which generates no additional significant issues.

The example structures investigated below illustrate the results from multiband band structure computations also.

4.2. Further considerations

The effect of exchange and correlation[39] due to electron–electron interactions can be taken into account through numerical calculations. The full electrostatic potential energy

$$V_{ch} = -|e|\,\phi_{ch}(z) + V_{ex}(z)$$

has the electron–electron exchange and correlation effects in the local density approximation [40, 41] given by

$$\begin{aligned} V_{ex}(z) &= -\left[1 + 0.0545\ r_s\ \ln\left(1 + \frac{11.4}{r_s}\right)\right] \\ &\qquad \times(18/\pi^2)^{1/3} R_y^*, \end{aligned} \tag{48}$$

where

$$\begin{aligned} r_s &= \left[\frac{4}{3}\pi a^{*3} n_n(z)\right]^{-1/3}, \\ a^* &= \varepsilon\hbar^2/m^* e^2, \\ R_y^* &= m^* e^4/(2\varepsilon^2\hbar^2), \end{aligned}$$

and $n_n(z)$ is the electron charge density. Numerical calculations which have included the effects of V_{ex} show[16, 24, 41, 42] that these effects can be neglected at least in GaAs heterostructures with doping levels of about $10^{18}\,\mathrm{cm}^{-3}$.

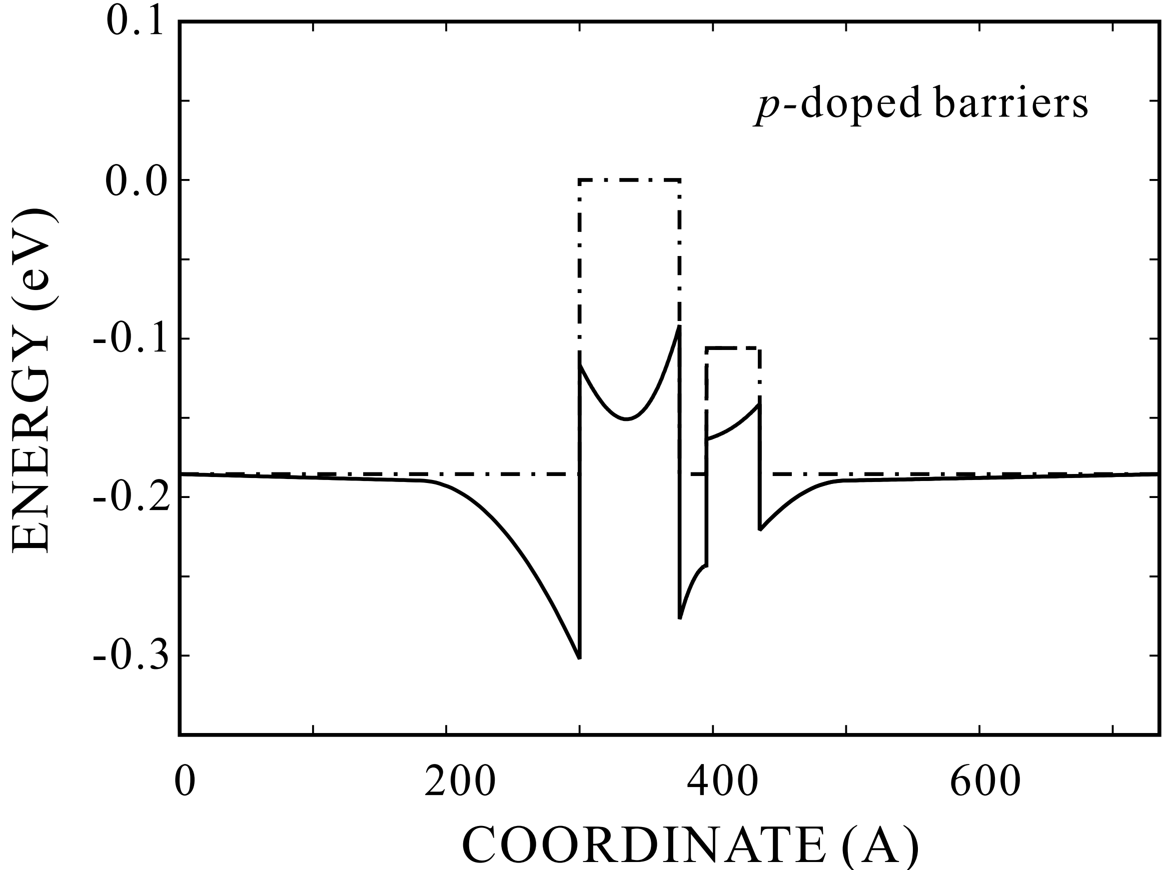

FIG. 4: The valence band bending in a double quantum well that is asymmetric due to the well widths and due to the Al content in the well layers is shown. The wells are 75 Å and 40 Å wide separated by a 20 Å barrier, all sandwiched between wide barriers, with Al content of all barriers being x=0.35. The narrower well is shallower, containing 20 % Al. The end barriers are p-doped with 1×10^{18} cm^{-3} impurity concentration while the middle barrier is p-doped with 1×10^{19} cm^{-3} impurities

4.3. Results

The structures we consider include p-type modulation-doped single quantum wells, a p-type modulation-doped asymmetric double quantum well, p-i-n-i superlattices, and n-type modulation-doped trilayer superlattices. These calculations are done at zero temperature. In the final example, we studied temperature effects in a n-type modulation-doped single quantum well. In all examples, GaAs and $Al_xGa_{1-x}As$ layers are used, and input material parameters are taken from Ref. 27.

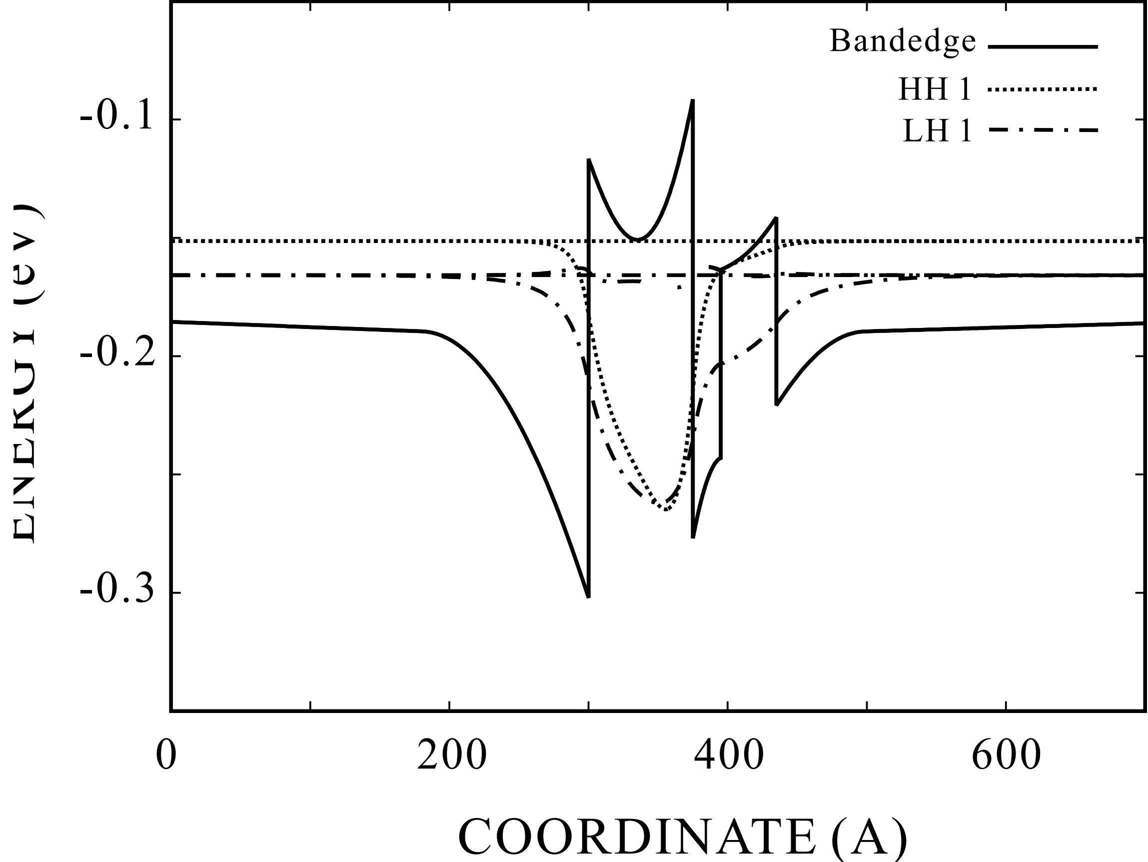

FIG. 5: The first heavy hole and light hole wavefunctions in the asymmetric double quantum well of Fig. 4 are shown. Since this calculation used the 6 band $\mathbf{k}\cdot\mathbf{P}$ model including heavy hole, light hole and spin-orbit split-off bands, the light hole wavefunction has a large light hole basis component and a small spin-orbit split-off basis component. At zero inplane wavevector, the heavy hole components are completely decoupled from the others.

4.3.1. A single quantum well with p-type modulation doping

We calculated the selfconsistent potential of p-type modulation-doped $GaAs/Al_{0.35}Ga_{0.65}As$ single quantum wells at two p-doing concentrations, 10^{19} cm^{-3} and 10^{17} cm^{-3}. In Fig. 1, the degenerate heavy-hole and light-hole band edges and the spin-orbit split-off band edge are shown. V_0 is the initial potential due to band offset, and the solid and dotted lines represent the selfconsistent potential for p-doping levels of 10^{19} cm^{-3} and 10^{17} cm^{-3}, respectively. As expected, the width of depletion region is shorter for higher doping; about 25 Å for $p = 10^{19}$ cm^{-3} case and over 200 Å for $p = 10^{17}$ cm^{-3} case. The band bending effectively gives rise to a symmetric double quantum well and this is

reflected in the behavior of the wavefunctions. In Fig. 2 we show the lowest two heavy hole states. The ground state happens to be higher in energy than the peak of the potential in the quantum well and it clearly shows a double peak.

Figure 3 shows a typical convergence behavior in a semilog scale. The inner iterations converges to below 10^{-5} eV after a few hundred iterations, while the outer iterations converge after a few tens of iterations. In general, the convergence is faster if the free carrier concentration is smaller.

4.3.2. A p-type modulation-doped asymmetric double quantum well

In Fig. 4 we show the selfconsistent potential for an asymmetric double quantum well of $Al_{0.35}Ga_{0.65}As$/GaAs(75 Å)/$Al_{0.35}Ga_{0.65}As$(20 Å)/ $Al_{0.2}Ga_{0.8}As$(40 Å)/$Al_{0.35}Ga_{0.65}As$. The end barriers are p-doped at 10^{18} cm^{-3} while the center barrier is doped at $p = 10^{19}$ cm^{-3}. The left barrier, close to the wide and deep well, is depleted more than the right barrier and the center barrier is fully depleted. Fig. 5 shows the first heavy-hole and the first light-hole wavefunctions. The deeply confined heavy-hole is mostly confined is the wide well, while the light-hole has a substantial probability in the narrow well.

4.3.3. p-i-n-i superlattices

Next we consider the case of a *p-i-n-i* GaAs superlattice, each region being 50 Å. The band bending is displayed in Fig. 6. The dotted line is for $p = n = 10^{18}$ cm^{-3}. In this case, the Fermi level is around mid-gap and all the donors and acceptors are ionized, with the system attaining charge neutrality with no free carriers. At zero temperature there is a wide range of the Fermi level with which all the impurities are ionized and no free carrier states are occupied, and the exact position of the Fermi level is irrelevant. The solid line in Fig. 6 corresponds to the case of $p = 2 \times 10^{18}$ cm^{-3} and $n = 10^{18}$ cm^{-3}. Again there are no free carriers. In order to maintain the charge neutrality, only half of the acceptors should be ionized. Only one Fermi level which is close to the valence band edge satisfies the charge neutrality.

In Fig. 7 we show the first two conduction eigenenergies and eigenfunctions at zero superlattice wavevector ($q = 0$) in the case of $p = 2 \times 10^{18}$ cm^{-3} and $n = 10^{18}$ cm^{-3}. The

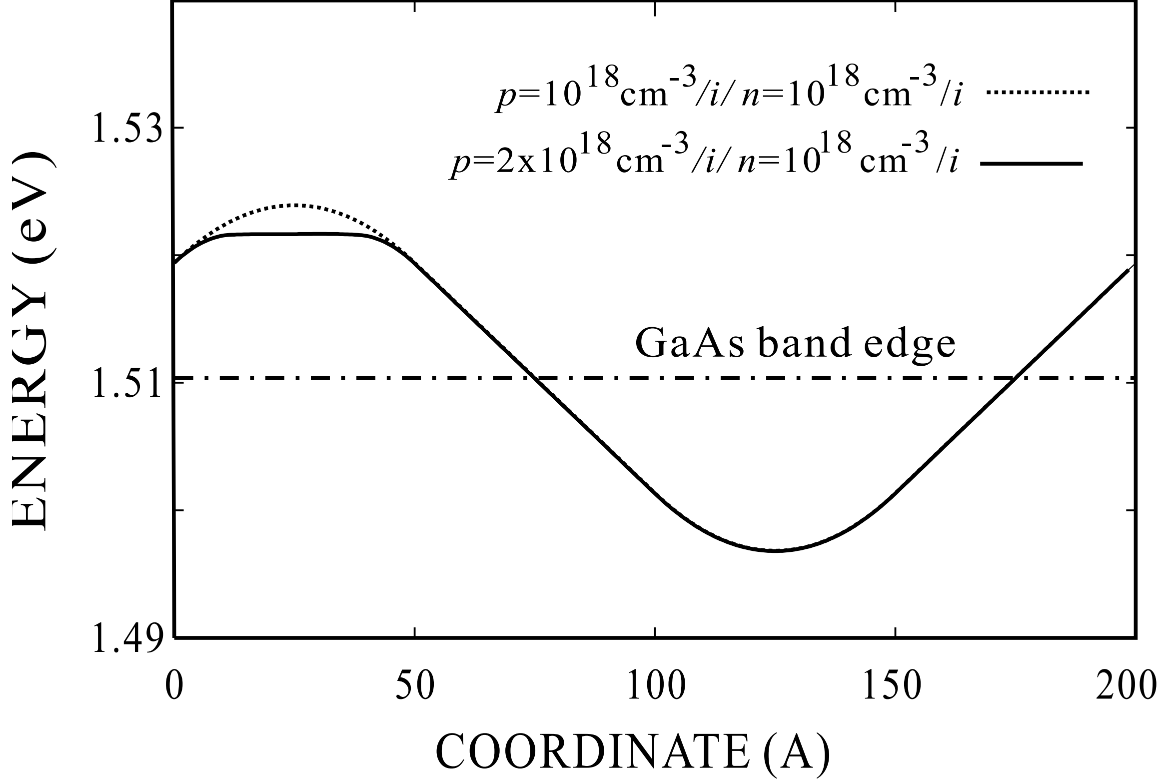

FIG. 6: The conduction band bending in a p-i-n-i GaAs superlattice with each region being 50 Å is shown. (i) The dotted curve corresponds to equal n and p doping at 1.0×10^{18} cm^{-3}, while (ii) the solid curve has twice the number of acceptor doping in the p-layers. The original GaAs band edge is shown for reference.

first conduction subband energy is below the maximum of the conduction band edge, but since the potential barrier in this p-i-n-i superlattice is not large, the wavefunction is relatively flat. The eigenenergy of the second subband energy is well above the maximum of the conduction band edge.

4.3.4. n-type modulation-doped trilayer superlattices

We considered band bending under selfconsistency in two trilayer GaAs(100 Å)/$Al_{0.2}Ga_{0.8}As$(50 Å)/$Al_{0.35}Ga_{0.65}As$(50 Å) superlattices where the $Al_{0.35}Ga_{0.65}As$ layer is doped with $n = 10^{18}$ and $n = 10^{19}$ cm^{-3}, respectively. In the $n = 10^{19}$ cm^{-3} case, the barrier is partially depleted and the Fermi level for the whole structure is the bulk Fermi level of the barrier region. On the other hand, in the $n = 10^{18}$ cm^{-3} case, the barrier is fully

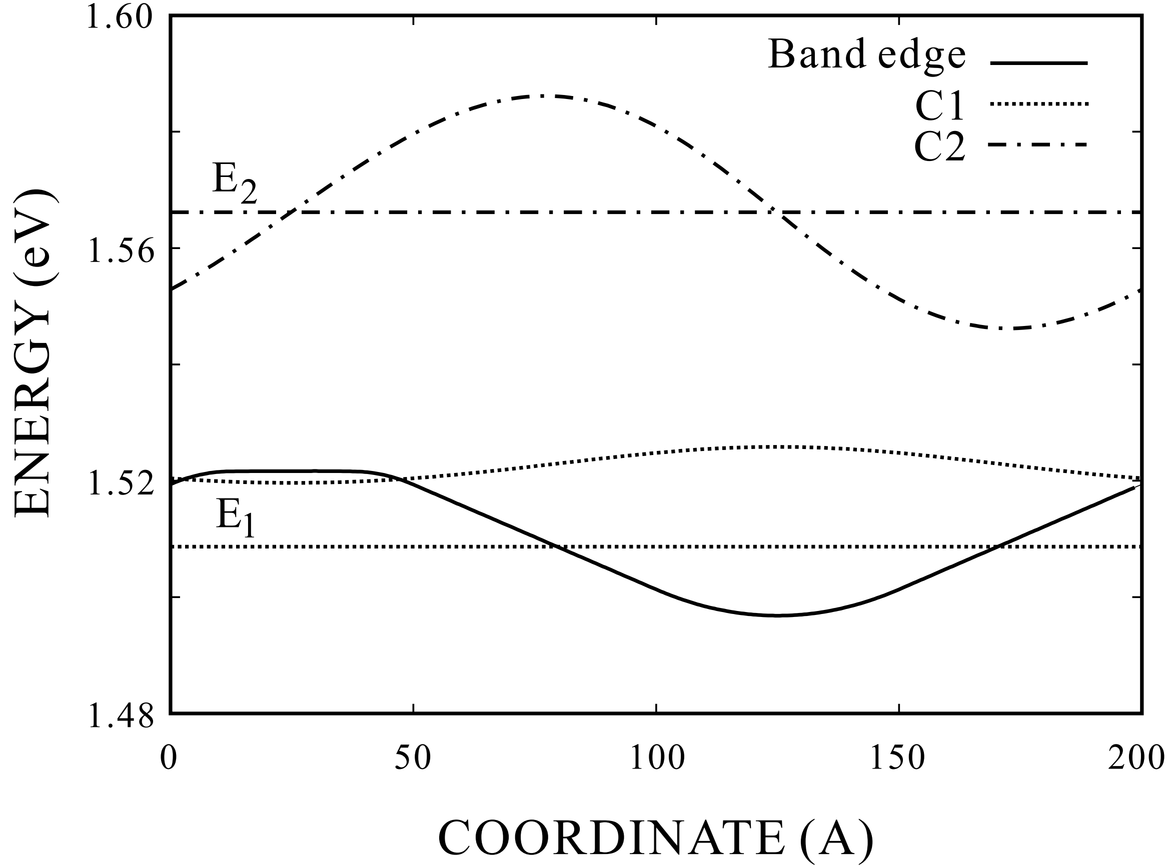

FIG. 7: The first two zone center energy levels and wavefunctions in the *p*-*i*-*n*-*i* GaAs superlattice of Fig. 6 are shown, together with the band edge (solid curve).

depleted and the Fermi level is determined to be at 1.666 eV. Figure 8 shows the selfconsistent potential of the two trilayer superlattices, and Fig. 9 shows the first two conduction subband wavefunctions at $q = 0$ for the $n = 10^{18}$ cm^{-3} case. Unlike the quantum well, the wavefunctions of the superlattice do not go to zero in the barrier region.

4.3.5. Effect of finite temperature

The variation of the selfconsistent potential with temperature for a modulation-doped ($n = 10^{18}$ cm^{-3}) GaAs/$Al_{0.35}Ga_{0.65}As$ single quantum well structure is shown in Fig. 10. As the temperature increases from 0 K to 100 K and to 300 K, the bandgap of both the well and barrier regions decreases, which accounts for most of the displacement along the energy axis. Beside this, the most significant effect is that the transition between the depleted and neutral barrier regions becomes smoother at higher temperature.

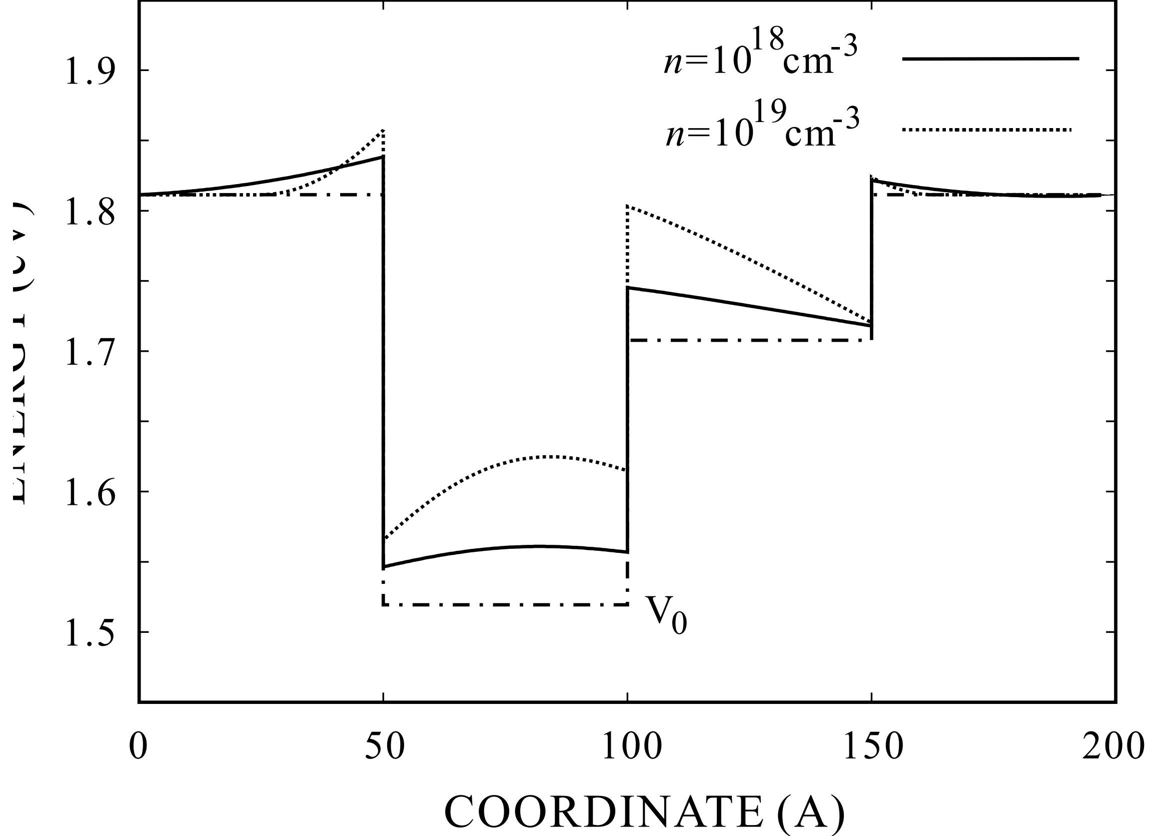

FIG. 8: The conduction band bending in a trilayer superlattice is shown. The superlattice consists of a 50 Å GaAs quantum well followed by a 50 Å layer of $Al_{0.2}Ga_{0.80}As$ and a 100 Å barrier of $Al_{0.35}Ga_{0.65}As$. The band edge is shown for a barrier n-doped to (1) 1.0×10^{18} cm^{-3} (solid curve) and to (2) $1.0{\times}10^{18}$ cm^{-3} (dotted curve). The 100 Å barrier is shown distributed symmetrically on both sides of the stepped quantum well. For 10^{18} cm^{-3} doping the barrier is completely depleted of unionized donors and the Fermi level is in the quantum well.

5. CONCLUDING REMARKS

We have shown that the finite element approach to the Schrödinger-Poisson selfconsistency calculations provides a controlled means of obtaining convergence in a fairly general manner. This has been illustrated in this thesis by several examples which bring out the nuances in the procedure.

The formulation presented here allows the generalization to numerically evaluating functional derivatives in the "weak" sense as a variational approach in which only the nodal values of the functions are varied in evaluating the derivative. This clearly has further

applications in the context of field theoretic calculations of physical quantities.

The calculation of the selfconsistent potential is a ubiquitous problem that occurs in every active quantum device. For example, the first step in multiband modeling of tunneling effects in layered structures is the determination of the band bending of the conduction and valence band edges under modulation doping. This includes the effect of strain and external electrically applied bias, and the effect of nonparabolicity in the in-plane energy band dispersion. The next stage is the computation of the multiband tunneling coefficient, which is then included in a tunneling current calculation. Again, in quantum well lasers, the energies of the actual energy levels employed in the lasing depend on the selfconsistent quantum well band profile. The problem is of central interest in layered spintronic semiconductor materials where the ferromagnetic behavior of Mn-doped layers is mediated by the free carriers interacting with the Mn spins through the exchange interaction. We hope to explore these problems in the near future.

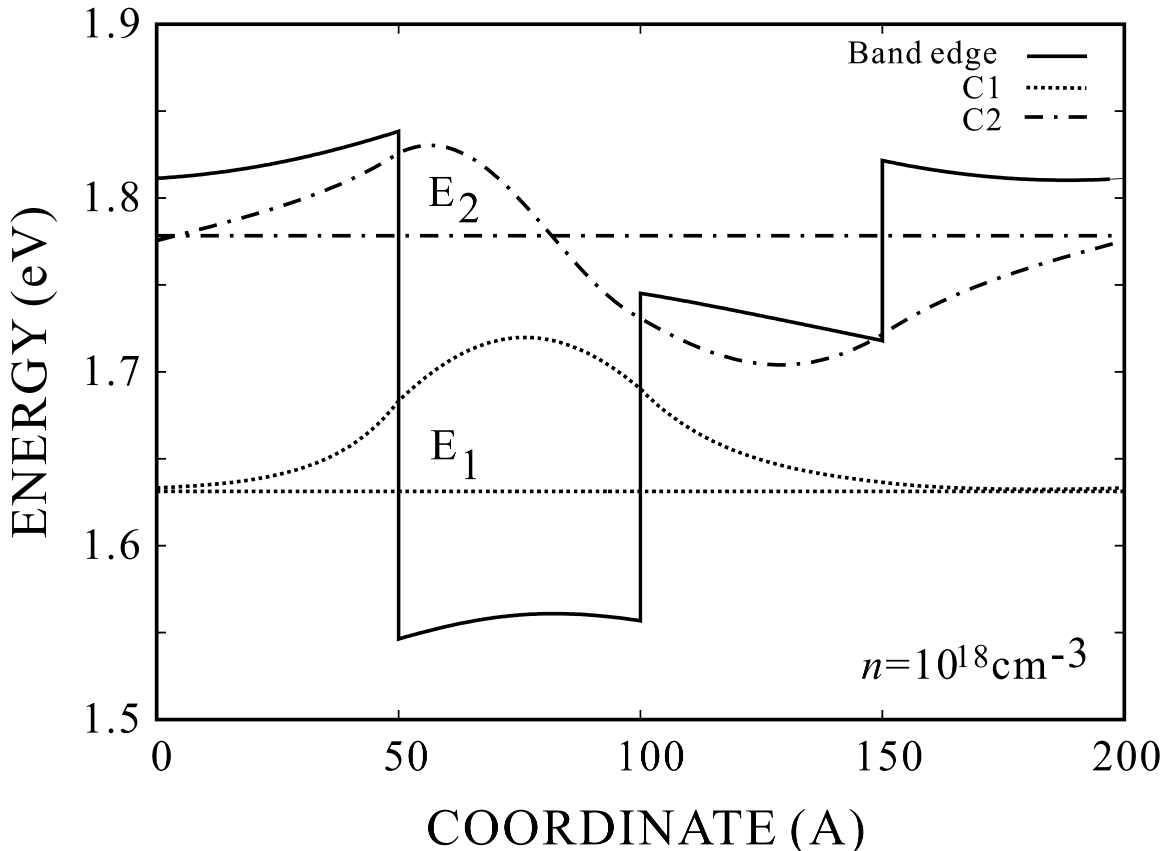

FIG. 9: The zone center energy levels and wavefunctions for the trilayer superlattice of Fig. 8 are shown with the band bending for $n = 1.0 \times 10^{18}$ cm^{-3}.

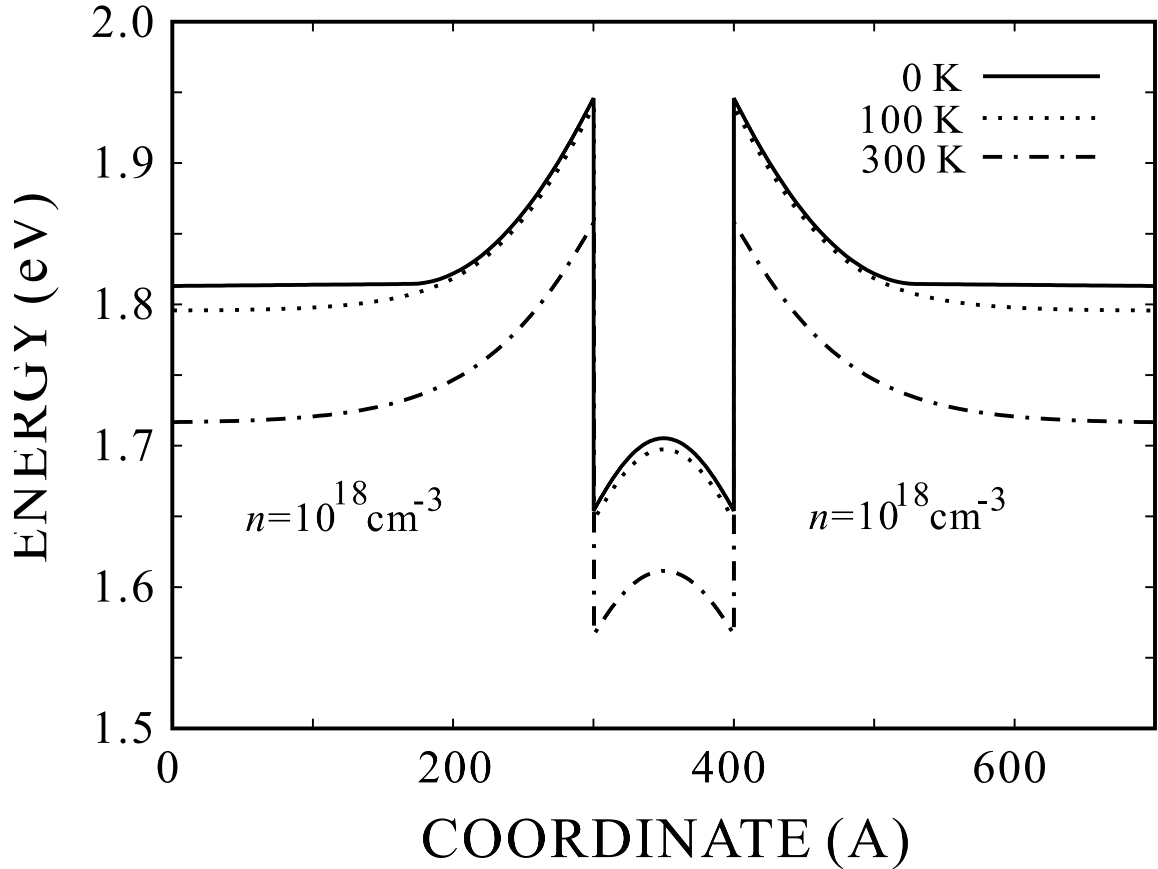

FIG. 10: The variation of the conduction band edge with temperature in a 100 Å GaAs quantum well structure. The reduction in the band gap with temperature has been included and the presence of free carriers above the band edge has been accounted for.

Bibliography

[1] L. R. Ram-Mohan, *Finite Element and Boundary Element Applications to Quantum Mechanics* (Oxford University Press, Oxford, 2002).

[2] O. C. Zienkiewicz, *The Finite Element Method* (McGraw-Hill, New York, 1989); O. C. Zienkiewicz and R. L. Taylor, *The Finite Element Method* (McGraw-Hill, New York, 1994).

[3] A Galerkin (B. G. Galerkin, Vestn. Inz. Tech. **19**, 897 (1915)) formulation employing the method of residuals within a FEM framework is an alternate approach to the solution of these differential equations; however, since both the Schrödinger and the Poisson

differential equations can be derived by applying variational principles to appropriate functionals the Galerkin and the variational approaches are equivalent. .

[4] B. C. Duncan, “Selfconsistent analysis of energy levels in modulation doped heterostructures” (Senior Thesis, Worcester Polytechnic Institute, 1990). A transfer matrix method was used for Schrödinger’s equation, and discretization with the “shooting method” for the Poisson problem – this procedure was observed to be unstable for high impurity concentrations $\geq 10^{18}\,\mathrm{cm}^{-3}$.

[5] T. Ando, A. B. Fowler, and F. Stern, Rev. Mod. Phys. **54**, 437 (1982).

[6] F. Stern, J. Comput. Phys. **6**, 56 (1970).

[7] I. Suemune, J. Appl. Phys. **67**, 2364 (1990).

[8] H. Mizuta and T. Tanoue, *The Physics and Applications of Resonant Tunneling Diodes* (Cambridge University Press, Cambridge, 1995).

[9] D. J. Rostcheck, “Selfconsistent calculations of electronic energy levels in quantum heterostructures” (Senior Thesis, Worcester Polytechnic Institute, 1992). The FEM was employed for both the Schrödinger and the Poisson equations, with quintic Hermite interpolation polynomials. The calculations were limited to a single modulation doped quantum well.

[10] A. Trellakis, A. T. Galick, A. Pacelli, U. Ravaiolli, J. Appl. Phys. **81**, 7880 (1997).

[11] G. Bastard, *Wave Mechanics Applied to Semiconductor Heterostructures* (Les Editions de Physique, Les Ulis, France, 1988).

[12] Ref. 1, *op. cit.*, Chapter III.

[13] R. P. Feynman, Phys. Rev. **56**, 340 (1939). H. Hellmann, in *Einfhrung in die Quantumchemie* (Deuticke, Leipzig, 1937), p. 285. For an application in the context of heterostructure bandstructure, see: L. C. Lew Yan Voon and L. R. Ram-Mohan, Phys. Rev. B **47**, 15500 (1993).

[14] Since setting the boundary nodal values to zero will reduce the dimension of the matrices by two, we employ a simple trick to retain the original matrix dimension: we zero the

leftmost and rightmost node's row and column corresponding to the end nodes in all the global matrices, and place a large number (say 10^3) at the diagonal entry in $A_{\alpha\beta}$ with unity for the diagonal entry in $S_{\alpha\beta}$. In effect, we have put the large matrices in a block-diagonal form such that the physically useful eigenvalues, which are of $\mathcal{O}(1)$ in eV units, will have eigenfunctions that are now zero at the ends. The two eigenfunctions with large eigenvalues are of course discarded.

[15] R. Shankar, *Principles of Quantum Mechanics*, 2nd ed. (Plenum, New York, 1994).

[16] T. Ando, J. Phys. Soc. Jpn. **51**, 3893 (1982); *ibid.*, **51**, 3900 (1982).

[17] G. Gilat and L. J. Raubenheimer, Phys. Rev. **144**, 390 (1966); Erratum Phys. Rev. **147**, 670 (1966).

[18] G. Lehmann and M. Taut, Phys. Stat. Sol. (b) **54**, 469 (1972).

[19] M. S. Methfessel, M. H. Boon, and F. M. Mueller, J. Phys. C **16**, L949 (1983).

[20] G. Wiesenekker, G. te Velde, and E. J. Baerends, J. Phys. C **21**, 4263 (1988).

[21] R. P. Brent, *Algorithms for Minimization Without Derivatives*, Chapters 3, 4 (Prentice Hall, Englewood Cliffs, NJ, 1973).

[22] F. Stern and W. E. Howard, Phys. Rev. **163**, 816 (1967).

[23] S. E. Laux, D. J. Frank, and F. Stern, Surf. Sci. **196**, 101 (1988).

[24] K. Inoue, H. Sakaki, J. Yoshino, and T. Hotta, J. Appl. Phys. **58**, 4277 (1985).

[25] The simultaneous equations are solved numerically using the upper triangular-lower triangular (LU)-matrix decomposition method of Gauss elimination for a sparse matrix representation of the matrices.

[26] J. M. Luttinger and W. Kohn, Phys. Rev. 97, 869 (1955).

[27] For a recent compilation of band parameters, see I. Vurgaftman, J. R. Meyer and L. R. Ram-Mohan, J. Appl. Phys. **89**, 5815 (2001).

[28] L. R. Ram-Mohan and J. R. Meyer, J. Nonlin. Opt. Phys. Mater. **4**, 191 (1995).

[29] L. R. Ram-Mohan, D. Dossa, I. Vurgaftman and J. R. Meyer, in *Handbook of Nanostructured Materials and Nanotechnology*, Vol. 2, Ed. H. S. Nalwa, (Academic Press, New York, 1999), Chap. 15.

[30] L. R. Ram-Mohan, I. Vurgaftman, and J. R. Meyer, Microelectronics Journal **30**, 1031 (1999).

[31] P. O. Lowdin, J. Chem. Phys. 19, 1396 (1951).

[32] E. O. Kane, J. Phys. Chem. Solids **6**, 236 (1958); E. O. Kane, in *Semiconductors and Semimetals*, Vol. 1, Ed. R. K. Willardson and A. C. Beer (Academic, NY, 1966); E.O. Kane, in *Handbook on Semiconductors*, Vol. 1 pg. 193, Ed. W. Paul (North-Holland, Amsterdam, 1982).

[33] M. G. Burt, Semicond. Sci. Technol. **2**, 460 (1987); Erratum **2**, 701 (1987); J. Phys. Condens. Matter 4, 6651 (1992).

[34] B. A. Foreman, Phys. Rev. B **48**, 4964 (1993).

[35] L. R. Ram-Mohan, unpublished lecture notes (1999).

[36] R. van Dalen and P. N. Stavrinou, Semicond. Sci. Technol. **13**, 1 (1998).

[37] D. L. Smith and C. Mailhiot Rev. Mod. Phys. **62**, 173 (1990).

[38] B. Chen, M. Lazzouni, and L. R. RamMohan Phys. Rev. B **45**, 1204 (1992).

[39] For the many-body theory of exchange and correlation effects see, for example, S. Raimes, *The Wave Mechanics of Electrons in Metals* (North-Holland, Amsterdam, 1961); A. L. Fetter and J. D. Walecka, *Quantum Statistical Mechanics of Many Particle Systems* (McGraw-Hill, New York, 1971); G. D. Mahan, *Many Particle Physics*, 2nd ed. (Plenum Press, New York, 1990); G. D. Mahan and K. R. Subbaswamy, *Local Density Theory of Polarizability* (Plenum Press, New York, 1990).

[40] O. Gunnarson and B. I. Lundquist, Phys. Rev. B **13**, 4274 (1976).

[41] T. Ando and S. Mori, J. Phys. Soc. Jpn. **47**, 1518 (1979).

[42] F. Stern and S. Das Sarma, Phys. Rev. B **30**, 840 (1984).